Physical Modeling and Numerical Simulation of Subcooled Boiling in One- and Three-Dimensional Representation of Bundle Geometry

by

M. Bottoni, R. Lyczkowski, and S. Ahuja
Argonne National Laboratory
9700 South Cass Avenue
Argonne, Illinois 60439

Submitted to 1995 ASME National Heat Transfer Conference
Portland, Oregon, August 5-9, 1995

Work supported by the U. S. Department of Energy

Physical Modeling and Numerical Simulation of Subcooled Boiling in One- and Three-Dimensional Representations of Bundle Geometry

M. Bottoni, R. Lyczkowski and S. Ahuja
Argonne National Laboratory, Argonne IL 60439-4825

Abstract

Numerical simulation of subcooled boiling in one-dimensional geometry with the Homogeneous Equilibrium Model (HEM) may yield difficulties related to the very low sonic velocity associated with the HEM. These difficulties do not arise with subcritical flow. Possible solutions of the problem include introducing a relaxation of the vapor production rate. Three-dimensional simulations of subcooled boiling in bundle geometry typical of fast reactors can be performed by using two systems of conservation equations, one for the HEM and the other for a Separated Phases Model (SPM), with a smooth transition between the two models.

1. Introduction

In the framework of safety analysis of liquid-metal-cooled fast reactors, the consequences of hypothetical core disruptive accidents must be evaluated. Accidents leading to loss of core integrity can be initialized by loss of flow (LOF) due to pump run-down, in concomitance with the failure of the reactor safety system to trip, or by transient over-power (TOP) reactivity excursion. In both cases, coolant boiling can be initialized in the core regions with the highest ratio of heat flux to coolant flow. Detailed knowledge about the spreading of the two-phase flow region within a reactor bundle is of paramount importance for feedback upon reactivity, which depends on the location of the bundle in the core layout. In conservative analysis of reactor cores, made with one-dimensional computer codes [1-2] and simulating a reactor bundle by a series of parallel equivalent channels, incoherence of boiling initiation between the different radial subchannels of a bundle could be investigated only in an approximate way, because the parallel channels are not coupled in the radial and azimuthal directions. For an accurate representation of the initial boiling phase, however, and for the simulation of its impact on the capability of reactor control, incoherence of boiling initiation must be taken into account. This can be done only with a three-dimensional representation of a reactor bundle provided by more advanced computer codes [3-4].

Incoherence of boiling initiation in reactor bundles is due to the existence of a subcooled boiling phase during which coolant vapor, produced in hot spots of a bundle, spreads into cooler regions and then condenses. This spreading of coolant vapor occurs predominantly in the radial, rather than the axial direction, with a relatively slow progression of the boiling front toward the outer bundle regions. Only when the vapor front has reached the outer hexagonal wrapper of a bundle is the bulk of the coolant on a cross section at saturation; the subcooled boiling phase then ceases. Nucleate boiling is then superseded by boiling in slug or annular flow regimes, and vapor expansion occurs predominantly in the axial bundle direction.

The purpose of this paper is to describe physical modeling and computational analysis of the initial subcooled boiling phase in a three-dimensional representation of a fast reactor bundle geometry. Boiling initiation, characterized by nucleate boiling regime, is naturally modeled by a slip model of coolant mixture. Problems related to the modeling and computational analysis of homogeneous flow, due to the existence of very low sonic velocity of the mixture at low qualities, are first examined in a one-dimensional test problem. Three-dimensional problems are then discussed. Because we are concerned with boiling development in several subchannels of a reactor bundle, and because different flow regimes can coexist in different adjacent subchannels, a model of separated phases is also considered in conjunction with the slip model.

This paper gives an overview of the conservation equations used for the mathematical description of boiling, with particular reference to the subcooled boiling phase, and summarizes the methods used for the numerical solutions. Discussion of the numerical simulation of a 7-pin and a 37-pin bundle is also presented. Some tentative conclusions are drawn.

2. Phenomenological Nucleation Theory

Let p_v be the vapor pressure inside a spherical bubble of radius r_b, and p_l be the pressure of the bulk of the liquid surrounding the bubble. For the bubble to exist and grow, the internal vapor pressure must overcome the forces of surface tension that tend to collapse it. Hence it must hold:

$$p_v - p_l \geq \frac{2\sigma}{r_b}. \tag{1}$$

The vapor pressure depends on the temperature at the bubble/liquid interface. Eq. (1) can be satisfied only if the interface temperature exceeds the saturation temperature corresponding to the liquid pressure; therefore the liquid surrounding the vapor must be superheated. This theory of homogeneous nucleation collapses for infinitesimal bubble radius, because it would then require infinite superheat for bubble generation. The physical argument to

justify the collapse of the theory of homogeneous nucleation is that the continuum representation does not hold for infinitesimal dimensions.

Thus, in real systems, nucleation must occur in the presence of impurity nuclei or at superheated walls with microcavities that trap nuclei of gases (heterogeneous nucleation). In the following, we will always refer to heterogeneous nucleation provided by superheated walls with given temperatures or heat fluxes. The excess pressure $\Delta p = p_v - p_l$ can be related to a wall superheat $\Delta T = T_w - T_s$ by the Clausius-Clapeyron equation:

$$\frac{\Delta p}{\Delta T} = \frac{h_{fg}}{T_s\left(\frac{1}{\rho_{gs}} - \frac{1}{\rho_{ls}}\right)}. \qquad (2)$$

Liquid sodium, the coolant we will consider in some of the applications, wets metal surfaces well and tends to dissolve surface impurities which de-activate nucleation cavities, thus leading to high wall superheat before boiling inception. Subcooled boiling initiated with large superheat will be considered in one of the numerical simulations.

3. Simulation of Subcooled Boiling Phase in Bundle Geometry

3.1. Phenomenological considerations

In subcooled boiling, there can be simultaneous evaporation at the base of a vapor bubble as it forms at a superheated surface, and condensation can occur at the top, immersed in subcooled liquid. We model this situation in the geometrical configuration of the pin bundles typical of fast breeder reactors. In typical reactor bundles with small pitch-over-pin-diameter ratio (p/D = 1.1-1.3) the gap between pins is ≈ 1-2 mm. Table I gives several examples.

Table I: Data of fuel assembly in some typical fast reactors.

p (mm)	D (mm)	p/D	Reactor
7.7	6.6	1.166	French Phoenix
7.9	6.0	1.316	German SNR-300
7.9	6.5	1.215	Japanese Monju
7.3	5.8	1.259	Clinch River Breeder, USA

Let us consider the simulation of a hypothetical power excursion accident due to loss of flow (LOF) or transient over-power (TOP) in the core of a fast reactor. In a hot spot in the narrow gap between rods of a reactor bundle, coolant reaches saturation and a vapor bubble grows rapidly in contact with the hot surface of the rod. As soon as the bubble fills the gap between rods, the vapor starts condensing as it contacts a cooler neighboring rod. Vapor therefore flows within a bubble from the hot to the cold surface. Heat of vaporization is transfer-

red to the vapor bubble through a liquid film, which becomes progressively thinner at the hot surface, and vapor condenses to form a progressively thicker film at the cold surface. As bubbles expand radially or axially into cooler regions, vapor at first condenses completely. This phase of subcooled boiling can only be simulated physically and computed numerically in a meaningful way, as explained later, with a full three-dimensional geometrical representation of the bundle geometry.

The initial phase of subcooled boiling has been simulated in bundle geometry by proceeding as follows:

- Solution of the momentum equation for a homogeneous mixture with slip and of the corresponding continuity equation yields the mixture velocity and vapor volume fraction. Assumptions about slip allow computation of both liquid and vapor velocities.

- When the real channel geometry is taken into account, the liquid phase is assumed to wet the pin surfaces by a liquid film. The thickness of the liquid film is computed. The vapor phase forms a bubble between the liquid films that wet the surfaces of two adjacent rods. This assumption is supported by experimental [5] and by theoretical investigations [6], which show that under conditions typical of fast nuclear reactor bundles, the growth of vapor bubbles in spherical form up to the size that fills the gap between rods occurs in a very short time, i.e., milliseconds.

- The initial vapor temperature inside a bubble is the superheated wall temperature at the location of nucleation. The vapor pressure is assumed to be the saturation pressure corresponding to that temperature. Initialization of a vapor bubble with large superheat thus implies a pressure peak in the location of the bubble formation. As the bubble expands into the subcooled liquid, the vapor condenses and pressure peak broadens and drops in amplitude thus allowing liquid film evaporation that sustains the pressure inside the bubble for a time. This subsequent evaporation sustained by pressure drop is referred to as flashing and plays a major role by the physical simulation of subcooled boiling. The analytical treatment that allows computation of mass transfer rate by evaporation or condensation due to pressure variations is given in Section 6.2 .

In the geometrical configuration typical of fast breeder reactor bundles, the subcooled phase is characterized by vapor bubbles expanding radially, rather than axially, toward cooler regions with lower heat fluxes. The radial vapor expansion is favored by the lower flow resistance in the radial rather than in the axial direction. As long as the bulk of the liquid coolant in a cross section of the bundle is below saturation, radial expansion implies vapor condensation in cooler regions, with slow progress of the vapor front into cooler domains. This flow pattern, characterizing subcooled boiling, lasts until the vapor front reaches the outermost cooler bundle regions, i.e., until the bulk of the coolant in the bundle cross section reaches saturation. At this point, the subcooled boiling

phase ceases and the vapor region begins to expand at a more rapid rate in the axial direction.

From the practical standpoint, the phase of subcooled boiling is characterized by a negative value of the mean thermodynamic quality over a bundle's cross section. Though lacking physical significance, this can be defined by:

$$x_B = \frac{h_{TP} - h_{ls}}{h_{gs} - h_{ls}}, \tag{3}$$

where h_{TP} ($< h_{ls}$) is the mean coolant enthalpy in a cross section, and subscript s refers to the liquid and vapor saturation lines. When the bulk of the liquid reaches saturation, x_B becomes positive and has the physical meaning of mean thermodynamic quality. In the following, however, we will not refer to x_B as defined above, but to the flowing quality:

$$x_{fl} = \frac{W_g}{W_g - W_l}, \tag{4}$$

defined as the ratio of vapor mass flow to the total mass flow across a given section. The flowing quality always has a physical significance.

In our approach to simulating the subcooled boiling phase and the subsequent transition to integral saturated boiling in bundle geometry, the following topics are therefore of paramount importance:

- Simulation of vapor expansion by a three-dimensional representation of the bundle: this implies that a full system of three-dimensional conservation equations for the liquid and vapor phases must be solved. In the subcooled boiling region, the volume fraction is generally small and a slip model for the mixture is appropriate. However, in the case of boiling inception with large superheat, large vapor volume fractions can be obtained. Thus, the simulation must proceed with a model of separated phases. A gradual transition between a slip model and a model of separated phases must occur in the regions where the vapor volume fraction exceeds a given threshold (typically 0.6).

- Modeling the interaction between liquid film and flowing vapor on both hot surfaces (film evaporation) and cold surfaces (film condensation); this is the liquid film model: When a model of separated phases is used for regions with void fraction larger than 0.6, friction coefficients at the liquid/vapor interface are computed and friction resistances are fed back to the solution of the momentum equations of the separated phases.

- Model of mass transfer due to pressure variations; this is the mass transfer model.

3.2. Geometrical Model

Selected experimental runs (which are presented later) were interpreted theoretically by using the two-phase flow capabilities of the BACCHUS-3D/TP computer code [4]. This program describes the thermal-hydraulic behavior of LMFBR rod clusters with a hexagonal pin arrangement under steady-state and transient conditions. The main characteristics of the code are summarized below.

The BACCHUS computer program has been structured to describe hexagonal arrangements of rods in bundles typical of LMFBRs. A complete reactor bundle, or a sector bounded by either ideal geometrical or material surfaces, can be described. Inlet and outlet bundle sections can be simulated. Additional options are provided for simulating unheated pins, pins with different diameters, displacements of pin axes, and grid spacers.

The local conservation equations describing the coolant flow are integrated over appropriate control volumes. Staggered meshes are used to define dependent variables (mass flows, pressure and enthalpy) and, correspondingly, different cells are used to achieve the macroscopic balances. The main control volumes ("centered cells") used for the mass and enthalpy balances are bounded (a) in the axial direction by two planes that are a distance Δz apart and perpendicular to the bundle z-axis; (b) in the radial direction, by planes through the pin axes Δr apart; and (c) in the azimuthal direction, by two planes passing through the bundle axis. The azimuthal direction is referred to as the s-coordinate. These main control volumes are shown in Fig. 1 for one-half of a 37-pin bundle divided into 12 azimuthal sectors. Up to 48 azimuthal sectors can be taken into account. The control volumes used for the balance of the scalar components of the momentum equations ("displaced cells") are formed by adjacent halves of two neighboring main control volumes. Scalar quantities (pressure, enthalpy, temperature, etc.) are defined in the midpoint of a centered control cell, whereas the scalar components of vector quantities (mass flows, velocities, etc.) are defined in the midpoints of the respective boundaries of the centered cell (which coincide with the midpoints of the displaced cells when equidistant spacing is used).

We impose pressure boundary conditions at the outlet of the bundle, and either pressure or velocity boundary conditions at the inlet. These boundary conditions are identical to those in experiments used to validate the code. Velocity boundary conditions at ideal geometrical surfaces or at material surfaces can be assumed with or without slip.

All cells are characterized by a total volume V, a volume occupied by the fluid V_f; an area A_w, of the solid wall/fluid interfaces, by areas of lateral faces S_β (the subscript β refers to the general coordinate direction); and by crossflow areas $S_{f\beta}$. For every cell, we define the surface permeabilities, $\gamma_\beta = S_{f\beta} / S_\beta$, as the ratio of the respective flow area to the total area. The volume porosity $\varepsilon = V_f / V$ of a cell is defined as the ratio of the volume occupied by the fluid to the total

cell volume. In an undisturbed geometry, volume porosity is equal to surface permeability in the axial direction.

An equivalent fuel pin, with geometrical data corresponding to those of real pins, is associated with every main control volume. For every equivalent pin, we consider the heating element (fuel or electrical heater) and a cladding that is separated from the fuel by a gap of given width. In the axial direction, gas plena, fission and blanket zones can be represented with different material properties.

4. Conservation Equations

As explained above, subcooled boiling generally occurs at low or moderate void fractions and can be simulated by a slip model for the fluid mixture. However, when boiling inception occurs with large superheat, a model of separated phases is necessary because vapor production can be very large locally. In this case, we need to solve both systems of conservation equations presented hereafter and provide cell-by-cell a smooth transition between the two models.

4.1. Slip Model (SM)

The governing equations for the conservation of mass, momentum and energy of the coolant for the slip model are as follows:

Continuity equation:

$$\frac{\partial \rho_m}{\partial t} + \nabla \cdot (\rho_m \vec{v}_m) = 0; \tag{5}$$

Momentum equation:

$$\frac{\partial (\rho_m \vec{v}_m)}{\partial t} + \nabla \cdot (\rho_m \vec{v}_m \vec{v}_m) + \nabla \cdot \left[x(1-x) \rho_m \vec{V}_{Sl} \vec{V}_{Sl} \right] = -\nabla p + \nabla \cdot (\mu_m \nabla \vec{v}_m) + \rho_m \vec{g} - \vec{D}_o; \tag{6}$$

Energy equation:

$$\frac{\partial (\rho_m h_m)}{\partial t} + \nabla \cdot \left(\rho_m \vec{v}_m \vec{h}_m \right) + \nabla \cdot \left[x(1-x) \rho_m \left(h_g - h_l \right) \vec{V}_{Sl} \right] = \frac{\partial p}{\partial t} + \vec{v}_m \cdot \nabla p + \left(\frac{1}{\rho_m} \right) \alpha_l \alpha_g \left(\rho_l - \rho_g \right) \vec{V}_{Sl} \cdot \nabla p - \nabla \cdot \vec{q} + Q. \tag{7}$$

In the equations, $\vec{V}_{Sl} = \vec{V}_g - \vec{V}_l$ is the slip velocity; if $\vec{V}_{Sl} = 0$, Eqs. 5-7 represent, as a subcase, the Homogeneous Equilibrium Model (HEM). Definitions of the symbols are given in the nomenclature.

4.2. Separated-Phases Model (SPM)

A five-equation Unequal Velocity, Equal Phase Temperature (UVET) seriated two-phase continuum [7] model is applied. It is based on the same enthalpy equation as above and on the following continuity and momentum equations:

Continuity equations:

$$\frac{\partial \rho_l'}{\partial t} + \nabla \cdot (\rho_l' \vec{v}_l) = -M \tag{8}$$

and

$$\frac{\partial \rho_g'}{\partial t} + \nabla \cdot (\rho_g' \vec{v}_g) = M; \tag{9}$$

Momentum equations:

$$\frac{\partial (\rho_l' \vec{v}_l)}{\partial t} + \nabla \cdot (\rho_l' \vec{v}_l \vec{v}_l) = -\{[0, M]\vec{v}_l - [0, -M]\vec{v}_g\} + \nabla \cdot (\mu_l \nabla \vec{v}_l) - (1-\alpha)\nabla p + \rho_l' \vec{g} - K(\vec{v}_l - \vec{v}_g) - \vec{D}_{ol} \tag{10}$$

and

$$\frac{\partial (\rho_g' \vec{v}_g)}{\partial t} + \nabla \cdot (\rho_g' \vec{v}_g \vec{v}_g) = -\{[0, M]\vec{v}_l - [0, -M]\vec{v}_g\} + \nabla \cdot (\mu_g \nabla \vec{v}_g) - \alpha \nabla p + \rho_g' \vec{g} + K(\vec{v}_l - \vec{v}_g) - \vec{D}_{og}, \tag{11}$$

where ρ_g' and ρ_l' are the macroscopic densities defined as:

$$\rho_g' = \alpha \rho_g \tag{12}$$

and

$$\rho_l' = (1-\alpha)\rho_l, \tag{13}$$

respectively. The symbol [a, b] represents the maximum of the two real numbers, a, b.

Techniques used to provide cell-by-cell a smooth transition of the simulated boiling behavior from the slip model to the model of separated phases are described in detail in Ref. 8. Below, we report a one-dimensional application of the HEM for critical subcooled boiling made with the computer code COMMIX-2 [3] and two three-dimensional applications in bundle geometry, made with the computer code BACCHUS-3D/TP [4].

5. One-Dimensional Simulation with the Homogeneous Equilibrium Model

Sodium boiling at near-atmospheric pressure occurs in fast reactors cooled with liquid metal in the event of pump run-down during a real or simulated loss of flow (LOF) or transient over-power (TOP) accident. The analysis of low-pressure forced convection of flow boiling presents numerical difficulties. One reason for these difficulties is that pressure drop increases as boiling begins, giving the well-known S-shaped characteristic of pressure drop versus mass flow, which may lead to physical instabilities. A second difficulty is that the velocity of the two-phase mixture at boiling inception may exceed the speed of sound of the HEM. In the following, we analyze this second problem on the basis of one-dimensional numerical simulations of flow boiling experiments [9] used as a benchmark problem of the European Liquid Metal Boiling Working Group (LMBWG) [10].

Experiments in steady-state low-pressure sodium flow boiling were performed to obtain definitive pressure drop versus flow rate data in simple, well-defined geometries [9]. Round and annular flow channels were used, and one of the round-tube tests was chosen for simulation. The internal diameter of the round tube was 6 mm and the heated length was 1 m. A condenser mounted above the unheated region was kept at a cover gas pressure of 0.8 bar. Boiling was initiated by decreasing the flow rate at constant heat flux. The inlet sodium temperature was maintained at 585 ± 15°C. A series of runs at 127 W/cm^2 was chosen due to the large number of measurements (14) over the range of 0.5 to 5 m/s. Boiling was found to begin at 2.5 m/s. The reported nominal power level was 25 kW. The computer code used for the simulations was COMMIX-2 [3].

The problem was modeled in one-dimensional cylindrical coordinates with 52 axial nodes, each 4 cm high. The first 25 were heated and the next 25 unheated, followed by a one-node condenser and an unheated node. Heating was prescribed as a constant heat flux. The problem was first run with an inlet velocity fixed at 2.7 m/s at an inlet temperature of 570°C. After steady state was achieved, the inlet flow was decreased to 2.5 m/s over 100 time-steps of 0.01 s.

In the computer simulation, boiling occurred in only one axial mesh, and vapor recondensed just above the point of inception. The conditions were thus typical of subcooled boiling. Numerical difficulties occur at boiling via lack of convergence and physical instabilities. Also, flow oscillations were experienced. The compressibility of the flow mixture was, however, computed rigorously. Formal differentiation of the function $\rho_m = \rho_m(p, h_m)$ with respect to time gives

$$\left(\frac{\partial \rho_m}{\partial t}\right)^r = \left(\frac{\partial \rho_m}{\partial p}\right)_{h_m}^n \frac{p^r - p^n}{\Delta t} + \left(\frac{\partial \rho_m}{\partial h_m}\right)_p \frac{h_m^r - h_m^n}{\Delta t}, \qquad (14)$$

where r is an iteration index at time level t_{n+1}. As a possible source of instability, the mass flux was checked against the critical mass flux for the HEM.

It was found that the HEM's speed of sound and corresponding mass flux were greatly exceeded. The two-phase velocity was 10.6 m/s, while the mass flux was 3.49 x 10^3 kg/(m^2 s). The HEM speed of sound at 1 bar and at the limit to zero quality is only slightly greater than 1 m/s, while the corresponding mass flux is only about 900 kg/(m^2 s). The computed quality was x = 0.0004 which corresponds to a vapor volume fraction of 0.44.

To prove that the COMMIX-2 code is stable when the speed of sound is not exceeded, another simulation was performed. This was a one-dimensional representation of a 19-pin electrically heated steady-state test performed on the CFNa loop at Grenoble, France [11]. The conditions of the simulation were as follows: inlet temperature = 400°C; inlet velocity = 0.413 m/s; outlet pressure = 1.4 bar. Total power was 4.25 x 10^4 W. Twelve nodes were used in Cartesian coordinates. The first was 0.12 m high and the rest were 0.1 m high. The first node was adiabatic, the middle six nodes had a volumetric heat source of 4.17 x 10^8 W/m^3, and the last five nodes were adiabatic. All nodes were 0.13 x 0.13 m^2 in cross section. The flow was chosen so boiling occurred at the end of the heated region, in node 7. The results of the numerical computation are shown in Fig. 2, which plots pressure and void fraction distribution versus node number. Even though the void fraction changes from 0 to 0.95 in a single node, and the density changes from 740 to 47 kg/m^3, the results were stable. In this case, the HEM's speed of sound was never exceeded.

More details about applications of the COMMIX-2 code in critical and noncritical subcooled boiling are given in Ref. 12. The study reported in this reference shows that a critical state exists for the calculation of the pressure gradient in the frame of the HEM. The critical state can be avoided by forcing the flow to become sonic when it exceeds the HEM's speed of sound. This can be done by prescribing suitable values of pressure at the boundary of the computational domain. Another possible resolution of the problem is allowing for a certain amount of thermodynamic non-equilibrium, such as a boiling delay relaxation time, which raises the speed of sound, especially at very low qualities. From the computational standpoint this relaxation can be obtained by multiplying the derivative of the mixture density with respect to enthalpy, in Eq. 14, by a positive coefficient smaller than 1.

6. Three-Dimensional Modeling of Subcooled Boiling

As explained earlier, subcooled boiling is characterized by vapor flow from localized regions of high heat fluxes to cooler regions where vapor condenses. In liquid metal systems, as soon as the vapor quality increase above, say 10^{-4}, heat is transferred to the vapor through evaporation of a liquid film which becomes progressively thinner, and is released by condensation to a film which becomes thicker. Friction between liquid film and vapor flow is important for the solution of the momentum equations. The evaporation - condensation process is influenced by pressure variations. In this section we examine in some detail the sub-models for the liquid-film/vapor interaction and for simulating mass transfer due to pressure oscillations.

6.1. Liquid-Film/Vapor Interaction

Solution of the continuity equations yields the vapor and liquid volume fractions. The liquid volume fraction is modeled as an equivalent liquid film, the thickness of which is determined from the geometry of the simulated rods. Within the film, a velocity distribution given by the "universal velocity profile"

$$\begin{aligned} u^+ &= S^+ && S^+ \le 5 \\ u^+ &= -3.05 + 5 \ln S^+ && 5 < S^+ \le 30 \\ u^+ &= 5.5 + 2.5 \ln S^+ && 30 < S^+ \end{aligned} \qquad (15)$$

is assumed. u^+ and S^+ are the dimensionless velocity and film thickness, respectively, defined by

$$u^+ = u/u^* \qquad (16)$$

and

$$S^+ = Su^*/\nu \qquad (17)$$

where u^* is the friction velocity. The velocity distribution, Eq. 15, allows computation of the liquid-film velocity at the liquid-vapor interface $\vec{v}_{li}$, hence the shear stress:

$$\tau_i = \frac{\psi_i}{2}\rho_g\left|\vec{v}_g - \vec{v}_{li}\right|. \qquad (18)$$

The friction coefficient ψ_i can be computed by [13]:

$$\psi_i = \psi_g \phi_g^2 \alpha^{5/2}, \qquad (19)$$

where ψ_g is the friction coefficient for the case of the vapor flowing alone and ϕ_g is the two-phase pressure drop multiplier, which depends on the Lockhart-Martinelli parameter [14]. The shear stress, given by Eq. 18, allows computation of the drag function K appearing in the momentum Eqs. 10 and 11, by [15]:

$$K = \frac{2\psi_i \rho_g \left|\vec{v}_g\right|}{D_h \alpha}. \qquad (20)$$

More details about this computation are given in Ref. [16].

6.2. Mass Transfer Model

The mass of fluid transferred between the phases in the evaporation or condensation processes has been computed in Ref. [8] taking into account pressure variations in time and space. It is given by

$$M = \underbrace{\frac{1}{h_{fg}}\left(\phi - \frac{Q_l}{V_f}\right)}_{(a)} + \underbrace{\frac{B_g + B_l}{s_g - s_l}}_{(b)} - \frac{1}{h_{fg}}\left\{\frac{\partial p}{\partial t}\left[\alpha\rho_g \frac{dh_g}{dp} + (1-\alpha)\rho_l \frac{dh_l}{dp} - 1\right]\right.$$
$$\left. + \underbrace{\frac{\partial p}{\partial x_i}\left[\alpha\rho_g u_{gi}\frac{dh_g}{dp} + (1-\alpha)\rho_l u_{li}\frac{dh_l}{dp} - \left(\alpha u_{gi} + (1-\alpha)u_{li}\right)\right]}_{(c)}\right\} \qquad (21)$$

with the definitions:

$$B_l = -\nabla\cdot(1-\alpha)\vec{\varepsilon}_l + E_{sl} + (1-\alpha)D_{sl} \qquad (22)$$

$$B_g = -\nabla\cdot\alpha\vec{\varepsilon}_g + E_{sg} + \alpha D_{sg} \qquad (23)$$

and

$$\vec{\varepsilon}_k = \frac{\overline{X_k \frac{\vec{q}}{T}}}{\overline{\alpha_k}}, \qquad k = l,g \text{ (Entropy flux)} \qquad (24)$$

$$E_{sk} = \overline{\vec{q}\cdot\nabla\frac{X_k}{T}}, \qquad k = l,g \text{ (Interfacial entropy source)} \qquad (25)$$

$$D_{sk} = \frac{1}{\overline{\alpha_k}}\left(\overline{\frac{X_k}{T}(\vec{\vec{\tau}}:\nabla\vec{v})}\right), \quad k = l,g \text{ (Entropy source due to viscous dissipation)} \qquad (26)$$

where overbars denote mean values over a computational cell. $X_k = X_k(\vec{x},t)$ is the "phase indicator function" with a value of 1 or 0, according to whether the point $\vec{x}$ lies within or outside phase k.

Term (a) in Eq. (21) gives the mass transfer rate that would be generated if only the heat transfer through the liquid film were considered. Using the definitions given in Eqs. 22 and 23, we rewrite term (b) in Eq. 21 as

$$\text{Term (b)} = \frac{B_g + B_l}{s_g - s_l} = \frac{1}{s_g - s_l}\left\{-\nabla\cdot\left[\alpha\vec{\varepsilon}_g + (1-\alpha)\vec{\varepsilon}_l\right] + E_{sg} + E_{sl} + \alpha D_{sg} + (1-\alpha)D_{sl}\right\}. \qquad (27)$$

Eq. 27 represents the rate of vapor mass generation by heat production due to conductive transfer (ε_k, E_{sk}) and viscous dissipation (D_{sk}). Term (b) is usually

smaller than term (a) but is not negligible with respect to term (c). Term (c) represents the contribution of time and space variation of pressure to the rate of vapor mass generation. If the pressure is constant in both time and space, term (c) vanishes. If heat power, term (a), is suppressed, term (c) becomes dominant because vapor production or condensation is then governed essentially by pressure variations.

7. Solution of Conservation Equations

7.1. Derivation of Pressure Equation

If Φ is denoted as a general variable, Eqs. 4-10 can be written in a generalized form as

$$\frac{\partial}{\partial t}(\rho\Phi)+\frac{\partial}{\partial x_i}(\rho u_i\Phi)=\frac{\partial}{\partial x_i}\left(\Gamma_\phi\frac{\partial\Phi}{\partial x_i}\right)+S_\phi. \tag{28}$$

Equation 28 can also be written more compactly as

$$\frac{\partial}{\partial t}(\rho\Phi)+\frac{\partial}{\partial x_i}\left(J_{\phi i}\right)=S_\phi \tag{29}$$

by using the definition of the total (convective plus diffusive) flux given by

$$J_{\phi i}=\rho u_i\Phi-\Gamma_\phi\frac{\partial\Phi}{\partial x_i}. \tag{30}$$

The diffusion coefficients Γ_ϕ and the source terms S_ϕ are specific to each meaning of Φ. Let us consider a control volume centered around node (i, j, k). Integration of Eq. 29 over this control volume and application of the divergence theorem yields:

$$\int_{V_f}\frac{\partial(\rho\Phi)}{\partial t}dV+\int_{A_{f,\beta+1/2}}J_{\phi\beta}dA-\int_{A_{f,\beta-1/2}}J_{\phi\beta}dA=\int_{V_f}S_\phi dV, \tag{31}$$

with β= (i, j, k). Next, the time-dependent terms are discretized. Using the definitions of the mean values of the fluxes J_ϕ's over the bounding surfaces and of mean values over the fluid volume V_f, we transform Eq. 31 into an algebraic equation for the seven unknowns Φ_β (β = 0, 1, ..., 6) at time level t_{n+1}:

$$a_o\Phi_o^{n+1}+\sum_{\beta=1}^{6}a_\beta\Phi_\beta^{n+1}=b_o^n. \tag{32}$$

Subscript o in Eq. 32 refers to the center node (i, j, k) considered, whereas indices (1, 2), (3, 4), (5, 6) refer to the neighboring nodes in the three coordinate directions, respectively. Equation 32 is formally identical with the equation that would be obtained by discretizing a Poisson equation $\nabla^2\Phi = b$. The only important difference is that the coefficients of the Poisson-like Eq. 32 do not depend on mesh size only, but also on convective and diffusive fluxes. The right-hand side of Eq. 32 collects all terms computed at time level t_n.

7.2. Alternating Direction Implicit (ADI) Method for Two-Phase Flow

The standard numerical solution of the discretized Poisson equation is based on matrix decomposition techniques that require a large computer core for the storage of the matrix coefficients. Computing time increases strongly with increasing problem size. For the Poisson equation describing the pressure distribution, obtained by combining momentum and continuity equations, we developed an alternative technique based on advanced variants of the ADI method, which was adapted for two-phase flow simulations.

When the compressibility terms are written explicitly, the Poisson equation for pressure is

$$a_o p_o^{n+1} + \sum_{\beta=1}^{6} a_\beta p_\beta^{n+1} = b_o + c_o, \tag{33}$$

where

$$a_o = \sum_{\beta=1}^{6} a_\beta + \frac{1}{\Delta t}\left(\frac{\partial \rho_m}{\partial p}\right)_{h_m}^{n} \tag{34}$$

$$c_o = \frac{1}{\Delta t}\left[\left(\frac{\partial \rho_m}{\partial p}\right)_{h_m}^{n} p^n - \left(\frac{\partial \rho_m}{\partial h_m}\right)_{p}^{n}\left(h_m^{n+1} - h_m^n\right)\right]. \tag{35}$$

Let C be the diagonal matrix formed with the compressibility terms

$$c_m = \frac{1}{\Delta t}\left(\frac{\partial \rho_m}{\partial p}\right)_{h_m}^{n} \tag{36}$$

that appear in Eq. 34. The Poisson equation can then be written as:

$$\left(A_z + A_s + A_r + C\right)P = B \tag{37}$$

where the matrices A_z, A_s, A_r are formed with the coefficients that refer to the respective coordinate direction. A two-phase TP-ADI algorithm can be written:

$$(A_z + (1/3)C + zI)\phi^{(1)} = B - (A_z + A_s + A_r + C)P^n, \tag{38a}$$

$$(A_s + (1/3)C + zI)\phi^{(2)} = z\phi^{(1)}, \tag{38b}$$

$$(A_r + (1/3)C + zI)\phi^{(3)} = z\phi^{(2)}, \tag{38c}$$

$$P^{n+1} = P^n + 2\phi^{(3)}, \tag{38d}$$

and

$$z = r_L + m\frac{(c_m)_{\max}}{3}. \tag{39}$$

In Eqs. 38, ϕ represents an auxiliary vector indicating the residuals which vanish as the iteration converges. r_L is the optimization parameter that would be required for a single-phase flow calculation in the same geometrical configuration, and $(c_m)_{max}$ is the maximum of the compressibility terms, Eq. 36, in the computational domain. In all cases computed, the coefficient $m \geq 2$ ensured that the spectral radius of the iteration matrix of the scheme represented by Eqs. 38 was smaller than one. The computation of the optimal range of the parameter r_L and further details about this ADI-TP algorithm are given in Ref. [17]. This ADI scheme requires almost no additional core storage and can be vectorized to a high degree; for problems with more than about 5000 meshes, it is faster than every matrix decomposition technique.

8. Numerical Simulation of Subcooled Boiling in Bundle Geometry

8.1. Simulation of the NSK Series 7-pin Bundle Out-of-Pile Sodium Boiling Experiments

A number of sodium boiling experiments have been performed at KfK in the NSK (Natrium-Siede-Kreislauf) test loop, with a bundle of seven electrically heated pins within hexagonal wrappers simulating a fast reactor subassembly. The experiments of the series were intended to investigate the boiling behavior following a simulated failure of the power supply to the pumps coupled with coincident failure of the reactor to trip. The main purpose was to assess the boiling initiation in the different subchannels of the bundle and to analyze the rate of growth of the voided region and the onset of dryout in different subchannels. Detailed results of these experimental runs are given in Ref. 4.

As the experimental work was carried out in the frame of SNR development, the pin pitch (7.9 mm) and diameter (6 mm) correspond to those of the SNR-300 Mk-Ia fuel element. The pin surface heat fluxes were also in a range typical for SNR-300. However, the length of the electrically heated section was 600 mm,

compared with the fueled length of 950 mm of the SNR core. Power was constant along the axial height, compared to the cosine power distribution valid for reactor conditions. To compensate for these differences, test parameters such as coolant inlet temperature and outlet pressure were selected so that the axial temperature and pressure profiles at the onset of boiling were close to those calculated for a typical SNR subassembly.

In this section, we present numerical results of the simulation of experimental run 7-2/28, which is characterized by a superheat of 27 K at boiling inception. Characteristic data of this experiment are given in Table II. Results of the numerical simulation, up to the point of power switch-off and reestablishment of single-phase flow conditions, are also given in Ref. 4. In this section, we present results only for the subcooled boiling phase, which lasted about 1 s and is characterized by spreading of the vapor front mainly in the radial direction reaching the hexagonal wrapping. The phenomenological behavior of boiling in this case were explained in Section 3.1. Results of the numerical simulation, referring to the boiling phase, between $t \approx 1s$ and $t \approx 2s$, are shown in Fig. 3. The figure shows the spreading of the boiling region versus time in the innermost channels of the bundle, labeled IC = 1, and in the outermost channels, labeled IC = 2. For the innermost channels, a comparison with experimental values is available; the results show that as long as subcooled boiling lasts, there is incoherence of boiling in the subchannels of the bundle. Only when the two-phase flow region has spread over the full cross section of the bundle does vapor expansion become stronger in the axial direction. This trend becomes even more evident in the 37-pin bundle discussed in the next section. Analysis of the boiling incoherence is of paramount importance for reactivity feedback of the reactor due to sodium density changes, which are strongly space-dependent. Sodium loss from the center of the core yields highly positive reactivity effects, while sodium loss from near the core edge has negative reactivity effects.

Table II: Experimental data for NSK test run 7-2/28

Average steady -tate coolant conditions:	
Heat flux (W/cm^2)	152.6
Test section inlet/outlet pressure (bar)	2.19/1.05
Inlet/outlet temperature (°C)	559/730
Inlet coolant velocity (m/s)	3.02
Experimental conditions at voiding:	
Type of voiding initialization	Inlet valve blockage
Boiling inception (s)	0.95
Peak coolant temperature rise rate (K/s)	118
Coolant velocity at boiling inception (m/s)	0.0
Superheat (K)	27.0
Power switch-off (s)	3.22
Dry-out onset (s)	3.2
Duration of two-phase flow (s)	19.6

8.2. Simulation of the KNS-3 Series 37-Pin Bundle

As in the 7-pin bundle, several sodium boiling experiments were performed at KfK with a bundle of 37 electrically heated pins in the test section KNS-3 [18]. The main feature of this experimental series consists in the proper simulation of the cosine-shaped axial power distribution by means of oppositely developed electric heaters. The main aim of the 37-pin bundle experiments was the investigation of the (a) axial and radial coolant temperature profiles under steady-state and transient conditions, (b) the position and time of boiling initiation under loss of flow conditions and (c) propagation of boiling from central to peripheral subchannels [4]. In this case, six or twelve sectors were used for the azimuthal discretization. The spacer grids were simulated as flow resistances located between two meshes. The last spacer grid was shifted upstream by 50 mm to avoid flow perturbation and to coincide with the enlargement of the flow cross section. Flow through the mixer was modeled as one-dimensional and flow resistance was accounted for at the end of the last axial mesh. Pressure boundary conditions were imposed at the outlet and velocity and temperature were prescribed at the inlet.

Experimental run L58 was intended to simulate a situation similar to that during a very slow mass flow reduction typical of pool reactors. Experimental parameters of the L58 run are given in Table III.

Table III: Experimental data for KNS test run L58

Average steady -tate coolant conditions:	
Test section outlet pressure (bar)	1.0
Bundle inlet/outlet pressure (bar)	1.4361/047
Inlet temperature (°C)	600
Inlet coolant velocity (m/s)	1.9
Inlet mass flow (kg/s)	1.80
Heated Length (mm)	900
Average linear pin power (W/cm)	65.0
Total power (MW)	0.2167
Experimental conditions at voiding:	
Type of voiding initialization	Slow flow reduction
Boiling inception (s)	87.9
Coolant velocity at boiling inception (m/s)	0.61
Superheat (K)	0
Dry-out onset (s)	110.0
Power switch-off time(s)	114.2
Duration of two-phase flow (s)	32.1

The inlet mass flow run down was simulated by decreasing the pump power supply continuously. Axial and radial temperature distributions in the unheated region at boiling inception are shown in Fig. 4. The flatness is due to the combined effects of the slow mass flow reduction and high inlet temperature (600°C), this allows for prolonged heating of the uppermost pin section, which subsequently loses its cooling potential. As a consequence of this temperature

distribution just before onset of boiling, the two-phase flow region can be expected to propagate faster in the upward rather than downward direction. This was confirmed ex perimentally and through numerical computations.

Figure 5 shows the axial extension of the boiling region versus time in three of the four radial rings. It is evident that the time interval of boiling consists of two sequences: In the first phase, between onset of boiling and about 100 s into the transient, boiling expands strongly in the radial direction until the outermost ring, IC = 4, is reached; this first phase is the subcooled boiling phase. The second phase starts at about t = 100 s when the full cross section of the bundle is boiling, leading predominantly to axial vapor expansion.

9. Conclusions

The one-dimensional simulation of subcooled boiling with the Homogeneous Equilibrium Model (HEM), discussed in Section 5, points out the fundamental numerical difficulties encountered when the velocity of the two-phase flow mixture exceeds the HEM's speed of sound and the flow becomes critical. This is likely to occur in low-pressure boiling at very low qualities, because in these conditions the HEM's speed of sound is as low as 1 m/s. From the computational standpoint, flow oscillations and lack of convergence of the solution of the coupled conservation equations are experienced.

This paper points out the existence of the problem, which is often overlooked by code developers. The possible solution of the problem, probably also the most reliable one from the standpoint of physical representation of the flow, consists of forcing the flow to become sonic (or, to better express the physical reality, in simulating a physical situation in which the real speed of sound is higher than the value predicted by the HEM). This can be accomplished by allowing some degree of thermodynamical nonequilibrium between the phases, which decreases the peak rate of vapor generation and makes the vapor production more uniform in time.

It can be shown, both analytically and through computations, that multiplying the second derivative at the right-hand side of Eq. 14 by a positive coefficient of less than 1, introduces the desired relaxation of vapor production rate. This approach was followed and three-dimensional simulations were performed without numerical difficulties. However, when such difficulties do occur, the correct way to deal with them is unknown. More analytical work must therefore be dedicated to analysis of the problem if a sound theoretical foundation is to be found.

Nomenclature

A	surface area (m^2)
a	coefficient of Poisson equation (dimension given for pressure equation) (s/m^2)
B	entropy source defined by Eqs. 22 and 23 (W/m^3K)
b	right side of Poisson equation (dimensions given for pressure equation) (s/m^2)
C	diagonal matrix formed with compressibility terms (s/m^2)
c_m	compressibility of two phase mixture defined by eq. (36) (s/m^2)
D	entropy source due to viscous dissipation (W/m^3K) / pin diameter (m)
D_h	hydraulic diameter (m)
D_o	body force per unit volume(kg/m^2s^2)
E	Interfacial entropy source (W/m^3K)
$\vec{g}$	acceleration due to gravity (m/s^2)
h	specific enthalpy (J/kg)
h_{fg}	heat of vaporization = $h_{gs} - h_{ls}$ (J/kg)
h_m	specific mixture enthalpy = $xh_g + (1-x)h_l$ (J/kg)
I	identity matrix
J	convective plus diffusive flux (dimensions given for momentum flux) (kg/ms^2)
K	drag function (kg/m^3s)
M	mass transfer rate per unit volume (kg/m^3s)
p	pressure (N/m^2)
Q	power transferred to the coolant (W)
$\vec{q}$	energy flux (W/m^2)
r	radial coordinate (m)
S_ϕ	generalized source (dimensions given for momentum equation) (kg/m^2s^2)
S^+	dimensionless film thickness
s	azimuthal coordinate (m)
T	temperature (K)
t	time (s)
u	component of coolant velocity (m/s)
u^*	friction velocity (m/s)
u^+	dimensionless velocity
V	volume (m^3)
$\vec{v}, \vec{V}$	velocity vectors (m/s)
$\vec{v}_m$	mixture velocity = $x\vec{v}_g + (1-x)\vec{v}_l$ (m/s)
W	mass flow (kg/s)
X	phase indicator function
x	thermodynamic quality $= h_m / \left(h_{gs} - h_{ls}\right) = \rho_g' / \rho_m$

x_{fl} flowing quality = $W_m / \left(W_{gs} - W_{ls}\right)$
z axial coordinate (m)

Greek
α volume fraction of vapor
Γ diffusion coefficient (dimensions given for momentum equation) (kg/ms)
γ surface permeability
ε volume porosity
$\vec{\varepsilon}$ entropy flux (W/m^{2}K)
μ dynamic viscosity (kg/ms)
ν kinematic viscosity (m^2/s)
ρ microscopic density (kg/m^3)
ρ' macroscopic density (kg/m^3); $\rho'_g = \alpha\rho_g$; $\rho'_l = (1-\alpha)\rho_l$
ρ_m mixture density = $\rho'_g + \rho'_l$
σ surface tension (N/m)
$\vec{\tau}$ shear stress (kg/ms^2)
Φ transported scalar
ϕ specific power source (W/m^3)
ϕ^2 two-phase pressure-drop multiplier
ψ friction coefficient

Operators
$\nabla\cdot$ divergence
∇ gradient
$\frac{d}{dt}$ total derivative = $\frac{\partial}{\partial t} + \vec{v}\cdot\nabla$
[a, b] maximum of two real numbers a, b.

Indices
B bundle
b bubble
f fluid
g vapor
i dummy index/interface
k phase indicator
l liquid
m mixture
n superscript for time discretization
s saturation/entropy
Sl slip
TP twp phase
w wall
β dummy index

References

1. A. M. Tentner et al., The SAS4A LMFBR Whole Core Accident Analysis Code., Proc. Intl. Topical Meeting on Fast Reactor Safety, Knoxville, TN, April 21-25, 1985.

2. M. Bottoni, D. Struwe, BLOW-3A: A Theoretical Model to Describe Transient Two-Phase Flow Conditions in LMFBR Coolant Channels, KfK 3317, Dec. 1982.

3. M. Bottoni (compiler) et al., COMMIX-2: a Three-Dimensional Transient Computer Program for Thermal-Hydraulic Analysis of Two-Phase Flow, NUREG/CR-4371 Report, Argonne National Laboratory, ANL-85-47, Sept. 1985.

4. M. Bottoni, B. Dorr, C. Homann, The Three-Dimensional Transient Two-Phase Flow Computer Programme BACCHUS-3D/TP, KfK 4760, April 1992.

5. W. Peppler, Experimentelle Untersuchungen der Siedevorgaenge mit Natrium in engen Kanaelen und deren Anwendung auf schnelle Reaktoren, KfK - Ext. Bericht 8/72-1, Feb. 1972.

6. E. G. Schlechtendahl, Sieden des Kuehlmittels in natriumgekuehlten schnellen Reaktoren, KfK 1020, June 1969.

7. C. W. Solbrig and E. D. Hughes, Governing Equations for a Seriated Continuum: An Unequal Velocity Model for Two-Phase Flow, Two-Phase Transport and Reactor Safety, Vol. I, pp. 307-362. Hemisphere Publishing Corp., Washington, DC, 1978.

8. M. Bottoni and R. Lyczkowski, Modeling of Bubbly and Annular TwoPhase Flow in Subchannel Geometries with BACCHUS-3D/TP, Nuclear Technology 106 (1994), pp. 186-201.

9. C. Savatteri and H. M. Kottowski, Two-Phase Flow Liquid Metal Boiling Characteristics. Heat Transfer in Nuclear Reactor Safety, S. G. Bankoff and N. H. Afgan, eds., Hemisphere Publishing Corp., Washington, DC, 1982.

10. J. M. Seiler, Steady State Boiling Exercise, Proc. of the Liquid Metal Boiling Working Group, H. M. Kottowski and W. Peppler, eds., Karlsruhe, Germany, 1982.

11. A. H. Basque, D. Grand, B. Menant, Theoretical Analysis and Experimental Evidence of Three Types of Thermohydraulic Incoherency in Undisturbed Cluster Geometry, IAEA Specialists' Meeting on Thermodynamics of Fast

Breeder Reactor Fuel Subassemblies under Nominal and Non-nominal Operating Conditions, Karlsruhe, Germany, 1979.

12. R. W. Lyczkowski, H. Domanus, M. Bottoni and W. T. Sha, Analysis of Critical and Subcritical Flow Boiling, International Journal of Heat and Mass Transfer, Vol. 36 (1993), No. 15, pp. 3813-3822.

13. G. B. Wallis, One-Dimensional Two-Phase Flow, Mc Graw-Hill, 1969

14. R. W. Lockhart and R. C. Martinelli, Proposed Correlation of Data for Isothermal Two-Phase, Two-Components Flow in Pipes, Chemical Engineering Progress, Vol. 45 (1949), Nr. 1, pp. 38-49.

15. F. H. Harlow, A. A. Amsden, A Numerical Fluid Dynamic Calculation Method for all Flow Speeds, J. Comp. Phys. 8 (1971), pp. 197-213.

16. M. Bottoni and S. Ahuja, Use of Two-Phase Pressure Drop Multipliers and of ICE Technique in a Multi-Bubble Slug Ejection Model of Two-Phase Flow, Submitted for publication to Nuclear Science and Technology.

17. M. Bottoni, A Variant of the ADI Method for Two-Phase Flow Calculations, Computer and Fluids, Vol. 23 (1994), No. 2, pp. 305-321.

18. F. Huber, K. Mattes, W. Peppler and W. Till, Loss of Flow Experiments in Sodium with an Electrically Heated 37-pin Bundle with Sinusoidal Axial Heat Flux Distribution, ANS/ENS Intl. Top. Meeting on LMFBR Safety and Related Design and Operational Aspects, Lyon, France, July 19-22, 1982.

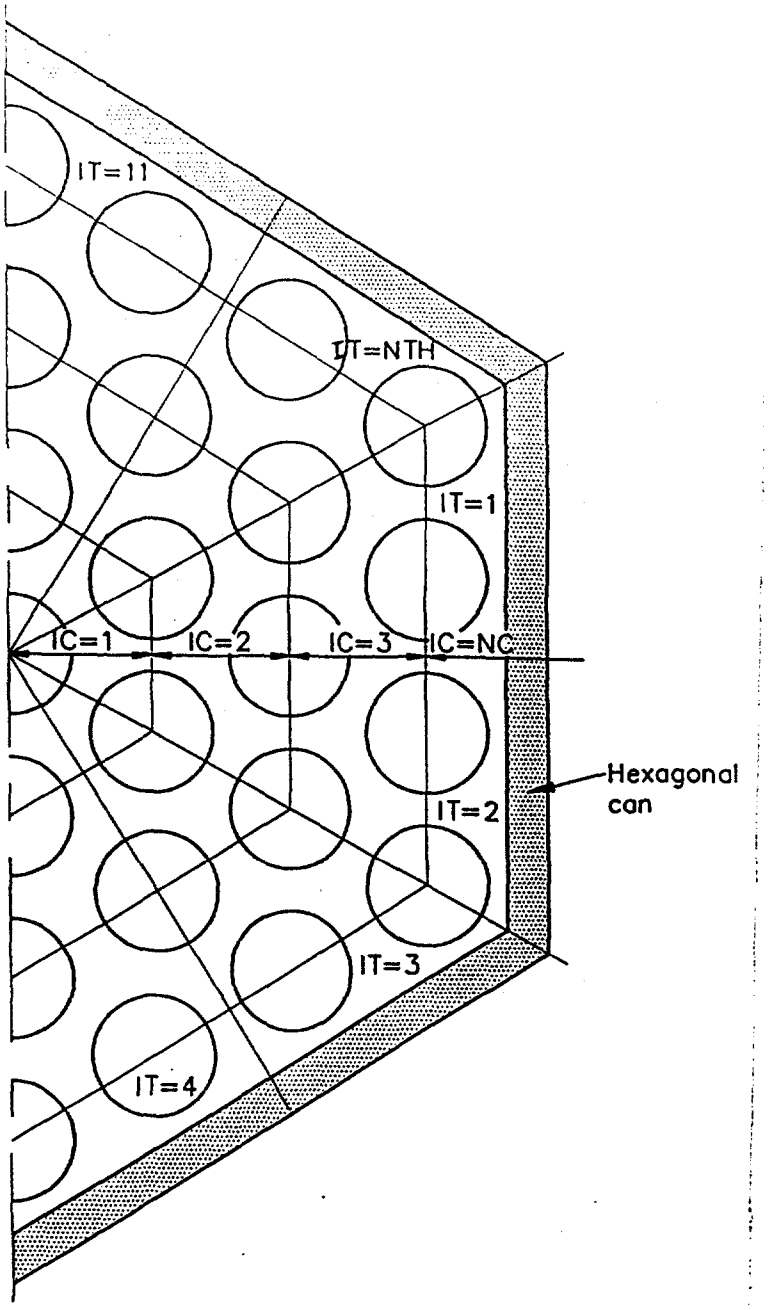

Figure 1: Control volumes and indexing conventions shown for one-half of 37-pin bundle. Indices IC (= 1,2, . . . , NC) and IT (= 1,2, . . . , NTH) refer to axial and azimuthal discretization, respectively.

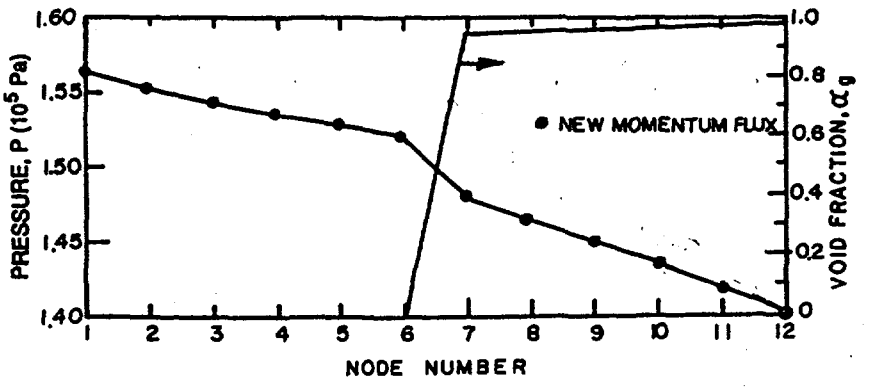

Figure 2: Plot of pressure and void fraction distribution versus axial discretization for one-dimensional model of Grenoble CFNa loop.

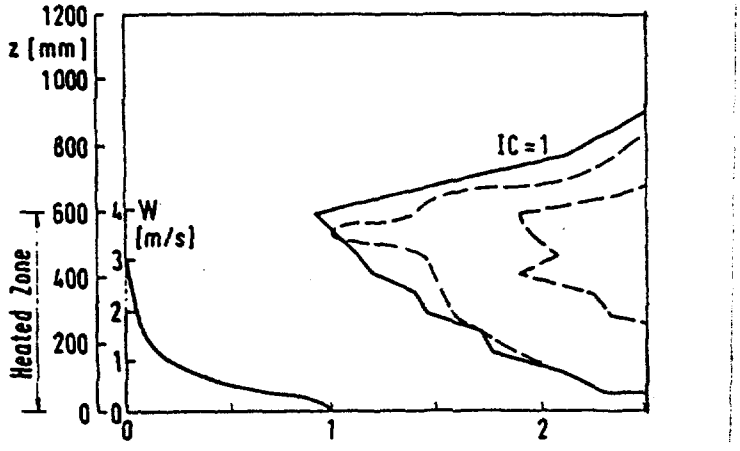

Figure 3: Experiment 7-2/28: Time variation of inlet velocity and comparison between experimental and calculated void region in inner (IC = 1) and outer (IC = 2) control cells.

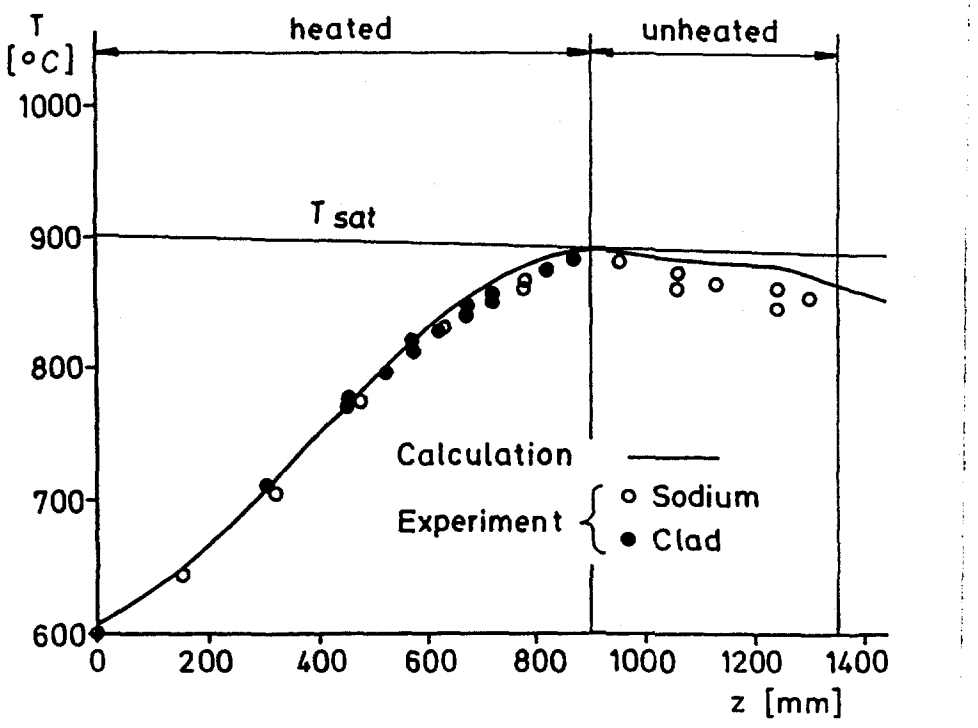

Figure 4: Measured and calculated axial temperature distributions in bundle center just before boiling inception for experiment KNS L58.

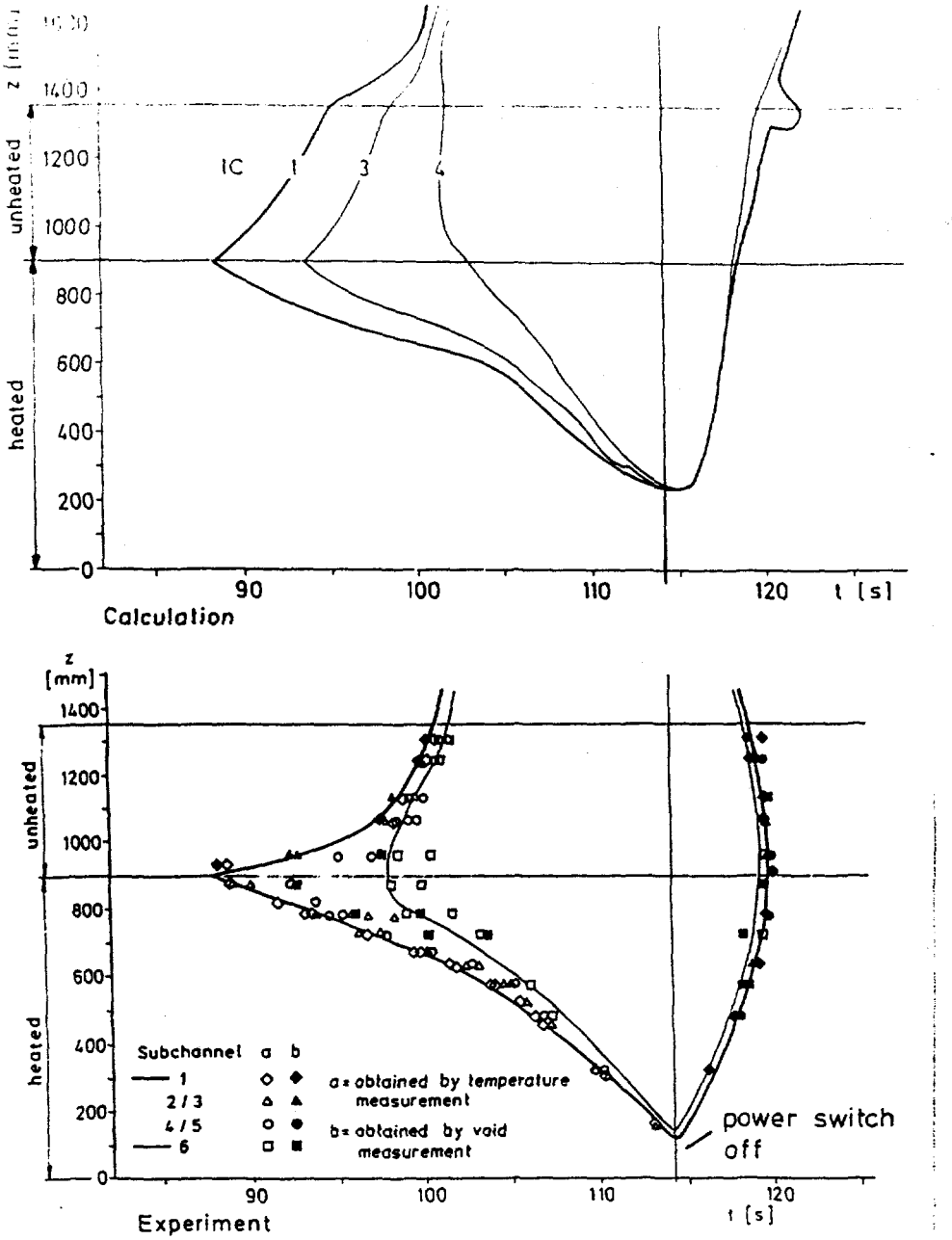

Figure 5: Measured and calculated development of boiling region for experiment KNS L58. The subcooled boiling phase occurs between 90 and 100 secs.